16th ICAAR LISBOA 2020-2022

16th International Conference on
Alkali-Aggregate Reaction in Concrete
Lisboa | LNEC | Portugal | 31 May - 2 June 2022

http://icaar2020-2022.lnec.pt

A plastic-damage model for concrete affected by alkali-silica reaction

Atila Sarikaya [(1)], Emre Erkmen [(2)], Nadarajah Gowripalan [(3)], Vute Sirivivatnanon [(4)]

(1) PhD Student, University of Technology Sydney, NSW, Australia, atila.sarikaya@uts.edu.au

(2) Assistant Professor, Concordia University, Montreal, Canada, emre.erkmen@concordia.ca

(3) Senior Research Fellow, University of Technology Sydney, NSW, Australia, nadarajah.gowripalan@uts.edu.au

(4) Professor of Concrete Engineering, University of Technology Sydney, NSW, Australia, vute.sirivivatnanon@uts.edu.au

Abstract

Deterioration of concrete due to alkali-silica reaction (ASR) is one of the problems that numerous concrete structures around the world have been suffering from. From the structural performance standpoint, the most detrimental product of ASR is the calcium silicate hydrate gel (ASR gel) which swells within the existing pores of the concrete. Expansion of the ASR gel induces significant stresses that may lead to cracks, spalling and deterioration in concrete.

A coupled elastoplastic-damage constitutive model (CEPD) of concrete is developed to predict the residual load carrying capacity and stiffness degradation of reinforced concrete structural elements affected by ASR. CEPD can capture the inelastic mechanical behaviour of materials by reflecting both stiffness degradation and permanent deformations. It is postulated that in the meso-scale, the expansion due to ASR is considered as an outcome of an internal ASR pressure, which introduces effective stresses when combined with load-induced stresses. The effective stresses are used to update the CEPD model parameters to define the inelastic evolution of the material. In order to determine the participation of ASR stresses into the effective stresses, a participation factor is proposed which is calibrated by considering free ASR expansion experiments. The model is implemented in a finite-element computer code, and obtained results are compared with those of experiments performed on a reinforced concrete beam.

Keywords: *alkali-silica reaction; coupled elastoplastic-damage; load-carrying capacity; modelling; reinforced concrete*

1. INTRODUCTION

ASR can impair the load-carrying capacity and serviceability of concrete structural elements. The deterioration in concrete is chiefly caused by silica gel, a product of ASR, which swells within the pores and cracks of concrete. While, in new structures, the occurrence and effects of ASR may be minimised by using non-reactive aggregates and cement, the problem for the existing structures that suffer from ASR persists. Therefore, the structural performance of such structures must be evaluated using proper models and techniques developed particularly for ASR-affected concrete.

Since ASR is a chemical reaction, one of the components of modelling of ASR is setting forth the reaction kinetics, which includes many factors such as temperature, water content, alkali content, type and size of reactive aggregate, porosity, stress state and diffusion mechanisms such as of heat and/or moisture. Another component of ASR modelling covers the mechanical behaviour of ASR-affected concrete that is mostly focused on deformations, stresses and degradation of material properties induced by the expansive nature of ASR. An inclusive model should embrace all the factors regarding chemical kinetics and mechanical behaviour. Some elegant examples include [1-6]. In this paper, our motivation is to predict the residual load-carrying capacity of ASR-affected structural elements. Therefore, in this study, we do not take into account reaction kinetics and we assume that the free expansion caused by ASR is known prior to analysis.

Considering the physical scales of the problem, modelling approaches to ASR can be classified into three groups, i.e., micro-, meso-and macroscale models [7], while different classifications can also be proposed such as that given in [8]. Microscale models typically consider a single aggregate with

surrounding cement paste. In mesoscale models, typically the interactions between a number of particles are considered, i.e. In order to predict global behaviour of ASR-impacted structures, macroscale models can be used due to their convenience of their framework which introduce stress, strain and stiffness degradation concepts. The proposed model in this paper covers macro and meso-scales.

Concrete is a heterogeneous material and its inelastic behaviour is complicated even when no detrimental effects such as ASR are taking place. Hence, mechanical modelling of concrete requires the implementation of sophisticated constitutive models. Among others, two main phenomenological approaches, i.e., plasticity and damage mechanics have been being utilised for prediction of inelastic response of materials. These methods have also been adopted for modelling of ASR-affected concrete. For instance, [4-6] can be given as plasticity-based examples while damage mechanics is utilised in [1,9], among many others.

While in the plasticity framework plastic (irreversible) deformations are in question, the degradation of material stiffness is sought in the damage mechanics framework. Many materials, including concrete, exhibit both characteristics in the inelastic region. Consequently, coupled plastic-damage models have been developed to predict the inelastic response of concrete, i.e., [10-13]. Among others, the work of Armero, Oller [14] was remarkable since they unified different damage models. In their framework, plasticity and damage components are iteratively enforced to produce the same stress update.

Based on the latter work, Sarikaya, Erkmen [15] introduced a novel ‘direct-coupling’ method and they applied it to concrete under compression. In their work, the total strain and the damage strain are interrelated by an a-priori relationship. Later, the method was extended to cover uniaxial tension and it was shown that the model was capable of capturing both hardening/softening response as well as stiffness degradation of concrete under tension-compression cyclic loads [16].

In this paper, the direct coupling framework of [15] is extended by implementing a novel three-surface plasticity model. The proposed multi-surface plasticity framework, as coupled with the damage framework, is an effective tool that can be utilised to investigate the mechanical behaviour of concrete under triaxial stresses. Similar to the method given in [16], a pair of damage variables, each for tension and for compression, are employed. The coupled elastoplastic-damage model is then employed in a two-scale analysis framework in which the pressures exerted by the development of ASR modify the effective stress on the elastoplastic-damage component of the model, and therefore, yield to irreversible deformations and stiffness degradation.

The outline of this paper is as follows: In the next section, we explain the method and underlying assumptions regarding ASR modelling. In Section 3, the direct plasticity-damage coupling method outlined in [15] is summarised and it is expanded to a multisurface plasticity framework. Section 4 is allocated for application of the coupled plasticity-damage model to concrete. In section 5, numerical examples are provided. Conclusions are presented in Section 6.

2. MODELLING OF ASR EFFECTS

In this study, we focus on two main characteristics of ASR’s effects on concrete, i.e., ASR-induced expansion and degradation of mechanical properties. We propose a constitutive model in which concrete is represented by an elastoplastic and damageable material that is subjected to ASR-induced and external load-induced stresses.

2.1 Assumptions regarding ASR evolution

As explained in the introduction, in this study, reaction kinetics is not considered and the ultimate free ASR expansion is assumed to be known prior to analysis. We also assume that no diffusion mechanism (i.e. temperature or moisture) is involved. These limitations narrow down the suitable structural element types to relatively thin and small ones where differences due to ASR expansion within an element may be considered negligible.

2.2 Constitutive model

The proposed constitutive model consists of two scales: the *meso-scale* and *macro-scale*. In the meso-scale, permanent deformations and degradation of the material is controlled by the effective stress. On the other hand, global strains and stresses are computed in the macro-scale. Figure 2.1 shows an

interpretation of a uniaxial model including the meso- and macro-scales, using rheological devices CEPD and ASR.

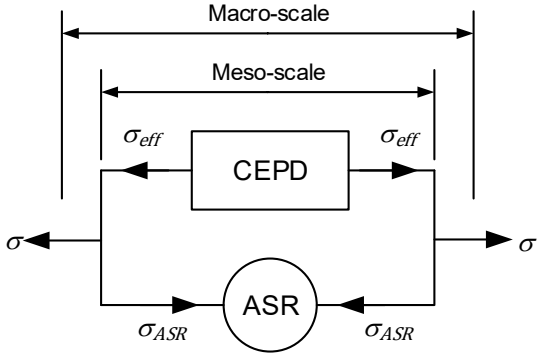

Figure 2.1: Rheological model with meso- and macro-scales – uniaxial stress case

In Figure 2.1, CEPD denotes '*coupled elastoplastic-damage device*' which is subjected to effective stress σ_{eff}, and ASR denotes a '*pressure device*' which generates the internal ASR pressure σ_{ASR}, and σ denotes the macroscopic stress in the macro scale. The effective stress acting on the CEPD device can be written in the tensor form, i.e.

$$\boldsymbol{\sigma}_{eff} = \boldsymbol{\sigma} + \boldsymbol{\sigma}_{ASR} \quad (1)$$

Similar to [6], the frictional mechanism activated by the swelling pressure of ASR is considered the same as those activated by applied stresses at material strength level. Therefore, in the proposed constitutive model, the inelastic response of the material is obtained from a single CEPD model regardless of the source of the effect, whether it is induced by ASR, external loads, or both.

It should be noted that the ASR-induced internal pressure $\boldsymbol{\sigma}_{ASR}$ acts as an eigenstress. The eigenstress can influence the material behaviour in the sub-scale while resulting in self-equilibrium in the macro-scale.

2.3 Coupled Elastoplastic-Damage Model (CEPD)

The CEPD is constituted of elastic, plastic and damage components, which are shown in the form of serially connected rheological devices in Figure 2.2. While the elastic device *E* provides the elastic response, the plastic dislocation device *P* produces the permanent deformations, whereas the damage device *D* modifies the stiffness of the system. The CEPD model is elaborated in Section 3.

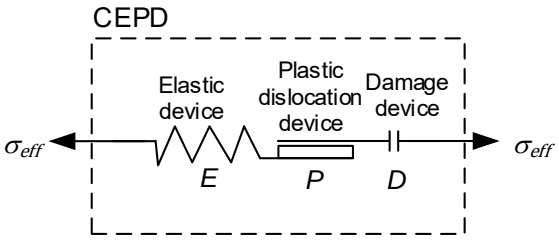

Figure 2.2: Interpretation of coupled elastoplastic-damage model – uniaxial case

2.4 Determination of ASR pressure

ASR pressure $\boldsymbol{\sigma}_{ASR}$ can be determined in a similar fashion to that of [6], i.e., by introducing the *porosity* and *reaction kinetics* into the system. However, here we follow a simpler approach based on free ASR expansion, as explained below.

Stage 0: Let us consider an externally loaded material with no ASR taking place. In this case, material parameters such as Young's modulus, compressive and tensile strengths and damage parameters can be calibrated based on the experimental data. As shown in Figure 2.3, the effective stress within the CEPD model is equal to external stress for this case, i.e. $\boldsymbol{\sigma}_{eff} = \boldsymbol{\sigma}$.

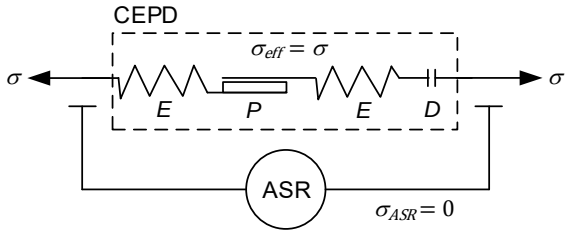

Figure 2.3: Uniaxial model with no ASR: Effective stress is equal to external stress.

Stage 1: Now, let us consider a concrete member subjected to ASR expansion only with no external loads and restraining effects (free expansion). In this case, the free expansion strain in ASR, $\boldsymbol{\varepsilon}_{ASR}^{Free}$, is applied simultaneously with the effective stress $\boldsymbol{\sigma}_{eff}$, as shown in Figure 2.4. Note that the effective stress is equal to ASR stress in free expansion case, i.e. $\boldsymbol{\sigma}_{eff} = \boldsymbol{\sigma}_{ASR}^{Free}$.

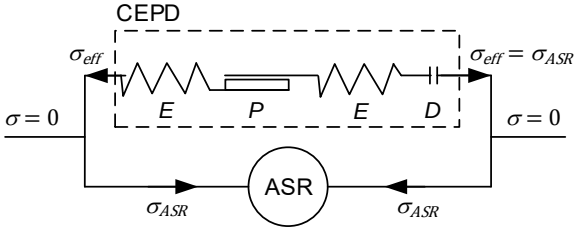

Figure 2.4: Uniaxial model with no external load (free ASR expansion).

By using the material parameters determined in Stage 1, model results can be compared with the data from free ASR expansion experiments in order to calibrate $\boldsymbol{\varepsilon}_{ASR}^{Free}$ and $\boldsymbol{\sigma}_{ASR}^{Free}$ to be used in the model. For instance, uniaxial stress-strain curves of ASR-impacted samples can be compared with model results. Here we propose a linear relationship between $\boldsymbol{\varepsilon}_{ASR}^{Free}$ and $\boldsymbol{\sigma}_{ASR}^{Free}$ i.e.

$$\boldsymbol{\sigma}_{ASR}^{Free} = \beta\, \boldsymbol{\varepsilon}_{ASR}^{Free} \tag{2}$$

in which $\beta \in [0,1]$ is a weighting factor to be calibrated by the experiments. When β is not zero, it updates the internal material parameters.

Stage 2: In the second stage, static analysis is performed based on the internal material parameters of the first stage. Both ASR strain $\boldsymbol{\varepsilon}_{ASR}$ and effective stress $\boldsymbol{\sigma}_{eff}$ persist in this stage so that the consistency between the stages is assured. It should be noted that while the effective stress $\boldsymbol{\sigma}_{eff}$ is utilised for the update of internal material parameters, the global stress $\boldsymbol{\sigma}$ is used for the global equilibrium in the coupled plastic-damage constitutive model explained in the next section.

3. COUPLED ELASTOPLASTIC-DAMAGE MODEL

3.1 Background: Sarikaya, Erkmen [15] – direct-coupling of plasticity and damage frameworks

In this paper, we follow the framework given in [15], in which plasticity and damage components are directly coupled in the constitutive model. In this method, the total strain tensor $\boldsymbol{\varepsilon}$ is decomposed into elastic ($\boldsymbol{\varepsilon}_e$), plastic ($\boldsymbol{\varepsilon}_p$) and damage ($\boldsymbol{\varepsilon}_d$) strain tensors, i.e.

$$\boldsymbol{\varepsilon} = \boldsymbol{\varepsilon}_e + \boldsymbol{\varepsilon}_p + \boldsymbol{\varepsilon}_d \tag{3}$$

Furthermore, the elastic domain is defined by the plastic and damage yield surfaces, which, contrary to other works such as [14] and [17], are kept equal in the direct coupling framework of [15], i.e.

$$f_p(\boldsymbol{\sigma}, \kappa_p) = f_d(\boldsymbol{\sigma}, \kappa_d) \leq 0 \tag{4}$$

where f_p and f_d denote plastic and damage failure criteria, respectively. The failure criteria are functions of plastic and damage hardening parameters, κ_p and κ_d, respectively.

The stiffness reduction in the material is represented by the area reduction factor $\varphi \in [0,1]$, or, by the damage parameter ϕ, which are interrelated with the equation $\phi = \varphi/(1-\varphi)$. Utilising the stored strain energy expression, one can obtain the stress-strain relationship as in [15], i.e.

$$\boldsymbol{\sigma} = (1-\varphi)\,\mathbf{E} : \left(\boldsymbol{\varepsilon} - \boldsymbol{\varepsilon}_{\mathrm{p}}\right) \tag{5}$$

and the relations between the strain components as

$$\boldsymbol{\varepsilon}_d = \varphi\left(\boldsymbol{\varepsilon} - \boldsymbol{\varepsilon}_p\right) \tag{6}$$

where $\mathbf{E}$ is the elastic stiffness tensor. Note that non-associated flow rules, i.e.

$$\dot{\boldsymbol{\varepsilon}}_p = \dot{\lambda}_p\, \boldsymbol{g}_{p,\boldsymbol{\sigma}} \tag{7}$$

$$\boldsymbol{\sigma}\,\dot{\phi} = \dot{\lambda}_d\, \mathbf{E} : \boldsymbol{g}_{p,\boldsymbol{\sigma}} \tag{8}$$

and other assumptions such as the equity of plastic and damage potentials, $g_p = g_d$, in [15] are utilised to obtain Eqs. (5) and (6). In Eqs. (7) and (8), $\dot{\lambda}_p$ and $\dot{\lambda}_d$ are the plastic and damage multiplier rates and g_p denotes the plastic potential function. The commas in the subscript indicate partial derivation, i.e., $\boldsymbol{g}_{p,\boldsymbol{\sigma}} = \frac{\partial g_p}{\partial \boldsymbol{\sigma}}$, and the superimposed dot $\dot{(\_)}$ denotes derivative with respect to time. Based on the assumption $\dot{\kappa_d} = \phi\,\dot{\kappa_p}$ the relation between the rates of plasticity multiplier and damage multiplier can be obtained, i.e.

$$\dot{\lambda_d} = \phi\,\dot{\lambda_p} \tag{9}$$

An important outcome of the direct coupling method in [15] is that damage components can be obtained directly from the plasticity computations because both plasticity and damage computations return the same stress increment. Therefore, no iteration between plastic and damage components is required to balance the stress.

In this study, we utilise the direct coupling method summarised above in order to determine the stiffness degradation in the compressive and tensile response of concrete. Therefore, in the following sections, the problem will be set mainly in the plasticity framework since the damage components can be obtained from corresponding plasticity components. Furthermore, since concrete's response to compression and tension is significantly different, a multi-surface plasticity framework is proposed in the next section in order to accommodate compression and tension characteristics in our constitutive model.

3.2 Multi-surface plasticity framework

For materials that behave significantly different in tension and compression, it is a convenient approach to utilise a set of yield surfaces in order to characterise the stress-strain evolution for each regime. In this paper, we introduce a novel three-surface multi-surface plasticity framework in order to cover both compression and tension characteristics of concrete.

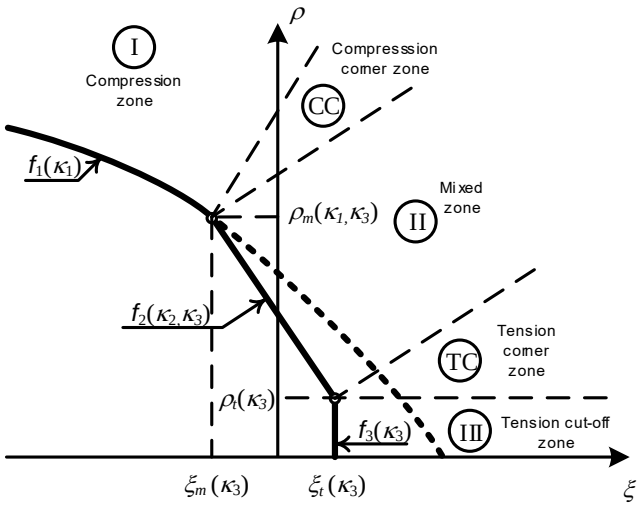

Figure 3.1: Three-surface composite yield surface – A Rendulic plane

The proposed three-surface plasticity framework covers yield functions of compression, tension and 'mixed' modes, constituting a composite yield surface. As shown in Figure 3.1, while the compression-mode yield surface f_1 is a nonlinear function of stress components, the tension-mode yield function f_3 is a vertical cut-off line in the Rendulic plane. Consequently, the tension cut-off surface limits the volumetric components of the stress tensor. The final component of the composite yield surface is the mixed-mode line, denoted by f_2.The mixed-mode yield line is constructed as a linear function which intersects the compression and tension cut-off functions at the prescribed stresses at points (ξ_t, ρ_t) and (ξ_m, ρ_m). For characterisation of hardening/softening effects during inelastic progression, hardening parameters κ_1, κ_2 and κ_3 are introduced. Therefore, yield functions can be expressed as

$$f_i = f_i(\xi, \rho, \theta, \kappa_i) \tag{10}$$

where, ξ, ρ and θ denote the Lode coordinates of the stress tensor $\boldsymbol{\sigma}$, and κ_i are the hardening parameters for $i = 1, 2, 3$. In the general sense, yield surfaces do not intersect smoothly and 'corner regions' occur in the stress space in which a uniquely defined gradient of the composite yield surface is not available [18]. Such regions, denoted by 'CC' and 'TC' (representing compression corner and tension corner, respectively), are demonstrated in Figure 3.1.

When hardening effects are present, the uniqueness of the multisurface plasticity solution is not guaranteed for all cases. In order to provide a unique solution, the linear complementarity problem (LCP) can be utilised. For instance, when two surfaces are active simultaneously, the LCP for the two-surface plasticity can be written following the procedure given in [19], i.e.

$$\mathbf{A}\,\dot{\boldsymbol{\lambda}} - \mathbf{b} \geq 0, \qquad \dot{\boldsymbol{\lambda}} \geq 0, \qquad \dot{\boldsymbol{\lambda}}^{\mathrm{T}}\left(\mathbf{A}\,\dot{\boldsymbol{\lambda}} - \mathbf{b}\right) = 0 \tag{11}$$

in which $(\_)^{\mathrm{T}}$ denotes the matrix transpose operation and

$$\mathbf{A} = \begin{bmatrix} a_{11} & a_{12} \\ a_{21} & a_{22} \end{bmatrix} = \begin{bmatrix} \boldsymbol{f}_{1,\boldsymbol{\sigma}} : \mathbf{E} : \boldsymbol{g}_{1,\boldsymbol{\sigma}} + H_1 k_1 & \boldsymbol{f}_{1,\boldsymbol{\sigma}} : \mathbf{E} : \boldsymbol{g}_{2,\boldsymbol{\sigma}} \\ \boldsymbol{f}_{2,\boldsymbol{\sigma}} : \mathbf{E} : \boldsymbol{g}_{1,\boldsymbol{\sigma}} & \boldsymbol{f}_{2,\boldsymbol{\sigma}} : \mathbf{E} : \boldsymbol{g}_{2,\boldsymbol{\sigma}} + H_2 k_2 \end{bmatrix} \tag{12}$$

$$\mathbf{b} = \begin{Bmatrix} b_1 \\ b_2 \end{Bmatrix} = \begin{Bmatrix} \boldsymbol{f}_{1,\boldsymbol{\sigma}} : \mathbf{E} : \dot{\boldsymbol{\varepsilon}} \\ \boldsymbol{f}_{2,\boldsymbol{\sigma}} : \mathbf{E} : \dot{\boldsymbol{\varepsilon}} \end{Bmatrix} \tag{13}$$

$$\dot{\boldsymbol{\lambda}} = \begin{Bmatrix} \dot{\lambda}_1 \\ \dot{\lambda}_2 \end{Bmatrix} \tag{14}$$

in which f_i and g_i stands for yield and potential functions, $\mathbf{E}$ is the elastic material tensor, and $\dot{\lambda}_i$ are the plastic multiplier rates. Note that, for simplicity, $\mathbf{A}$, $\mathbf{b}$ and $\dot{\boldsymbol{\lambda}}$ are expressed considering two-surface plasticity only $(i = 1, 2)$, and they can be generalised to the three-surface case. In Eq. (12), H_i are the plastic moduli, i.e. $H_i = \frac{\partial f_i}{\partial \kappa_i}$ whereas the hardening factors k_i are selected as the trace of the potential functions, i.e. $k_i = \mathrm{tr}(\boldsymbol{g}_{i,\boldsymbol{\sigma}})$.

The LCP can be solved for $\dot{\boldsymbol{\lambda}}$ using $\mathbf{A}$ and $\mathbf{b}$. For $\dot{\boldsymbol{\lambda}}$ to be unique, the principal minors of the matrix $\mathbf{A}$ must be positive, i.e.

$$a_{11} > 0, \qquad a_{22} > 0, \qquad \det(\mathbf{A}) = |\mathbf{A}| = a_{11}\,a_{22} - a_{12}\,a_{21} > 0 \tag{15}$$

4. APPLICATION OF THE MULTI-SURFACE PLASTICITY MODEL TO CONCRETE

4.1 Compression zone

For compression zone formulations, we adopt the same yield function and hardening law as those employed in [15]. However, a simpler plastic potential function is utilised.

4.1.1 Yield Function

For the compression zone, the yield surface proposed by Menetrey and Willam [20] is employed, i.e.,

$$f_1(\xi, \rho, \theta, \kappa_1) = \frac{3}{2}\left(\frac{\rho}{f_c}\right)^2 + q_h m_0 \left(\frac{\rho}{f_c\sqrt{6}}\,r + \frac{\xi}{f_c\sqrt{3}}\right) - q_h q_s \leq 0 \tag{16}$$

where, f_c is the uniaxial compressive strength of concrete and $q_h(\kappa_1)$ and $q_s(\kappa_1)$ are the hardening and softening functions. The friction parameter m_0 and the polar radius $r = r(\theta)$ are taken as the same given in [15].

4.1.2 Hardening and softening law

In Eq. (16), it can be seen that q_h and q_s (hardening and softening functions, respectively), vary the shape and location of the compression yield surface. Here we adopt the hardening and softening functions proposed in [21], in which the hardening parameter κ_1 is taken as the volumetric plastic strain ε_v^p, i.e.

$$q_h(\kappa_1) = q_h(\varepsilon_v^p) = k_o + (1 - k_o)\sqrt{1 - \left(\frac{\varepsilon_{vo}^p - \varepsilon_v^p}{\varepsilon_{vo}^p}\right)^2} \tag{17}$$

$$q_s(\kappa_1) = q_s(\varepsilon_v^p) = \left(\frac{1}{1 + \left(\frac{n_1 - 1}{n_2 - 1}\right)^2}\right)^2 \tag{18}$$

in which k_o is the uniaxial concrete strain at the onset of plastic flow. Note that, either $q_h = 1$ or $q_s = 1$ condition is applied when softening or hardening takes place, respectively [21]. In Eq. (17), ε_{vo}^p is the threshold value for the volumetric plastic strain at the uniaxial concrete strength, i.e. $\varepsilon_{vo}^p = \frac{f_c}{E_c}(1 - 2\upsilon)$ where E_c and υ are the Young's modulus and Poisson ratio for concrete, respectively. The variables in Eq. (18) are defined as $n_1 = \frac{\kappa_1}{\varepsilon_{vo}^p}$, $n_2 = \frac{\varepsilon_{vo}^p + t}{\varepsilon_{vo}^p}$ and $t = \frac{f_c}{15000}$, in which, f_c is considered in MPa.

4.1.3 Potential function

For determination of flow direction, a linear potential function is utilised, i.e.

$$g_1(\xi, \rho, \kappa_1) = -B\frac{\rho}{f_c\sqrt{q_h\, q_s}} + \frac{\xi}{f_c\sqrt{q_h\, q_s}} \tag{19}$$

where B is a factor to be calibrated using the experimental data.

4.1.4 Damage Evolution

The damage evolution is adopted from [11], i.e.,

$$\varphi_1 = 1 - \exp\left(-C_1\frac{\kappa_1}{\varepsilon_{vo}^p}\right) \tag{20}$$

in which C_1 is a parameter to be calibrated using experimental cyclic compression data.

4.2 Tension cut-off zone

4.2.1 Yield function

For the tension cut-off zone, a volumetric cut-off yield function is utilised.

$$f_3(\xi, \kappa_3) = \frac{\xi - \xi_t}{f_c} \leq 0 \tag{21}$$

where

$$\xi_t(\kappa_3) = q_3\, \xi_{t0} \tag{22}$$

in which $q_3(\kappa_3)$ is the softening function for the tension cut-off zone and ξ_{t0} is the initial volumetric tensile cut-off stress. The tensile cut-off zone yield function is constrained by the tensile corner deviatoric stress ρ_t, so that $\rho \leq \rho_t$ in this zone, as shown in Figure 3.1. ρ_t is also affected by the softening in this zone, i.e.

$$\rho_t(\kappa_3) = q_3\, \rho_{t0} \tag{23}$$

where ρ_{t0} is the initial deviatoric tensile cut-off stress. Note that associated plasticity is considered in the tension cut-off zone, i.e.

$$g_3 = f_3 \tag{24}$$

4.2.2 Softening law

The softening law for the tension cut-off zone is

$$q_3(\kappa_3) = \exp(-\frac{\kappa_3}{n_3}) \tag{25}$$

in which n_3 is the material parameter that controls the steepness of the softening part of the uniaxial tension stress-strain curve.

4.2.3 Damage Evolution

The damage evolution is characterised by an exponential relationship, i.e.

$$\varphi_3 = 1 - \exp(-C_3\,\kappa_3) \tag{26}$$

in which C_3 is a parameter to be calibrated using experimental cyclic tension data.

4.3 Mixed zone

4.3.1 Yield Function

The yield function for the mixed zone is a linear function of the stress components, and it is determined through the "elastic prediction-plastic correction" stress return process in the plasticity computations. In this zone, we keep the stress return in the Rendulic plane of the trial stress $\boldsymbol{\sigma}^{tr}$, and therefore, the Lode angle is $\theta = \theta^{tr}$.

As it is geometrically interpreted in Figure 3.1, the yield line of the mixed zone f_2 can be constructed using the two 'endpoints' (ξ_t, ρ_t) and (ξ_m, ρ_m), i.e. the corner stresses. While the endpoint at the tensile corner is constrained by the imposed deviatoric stress limit ρ_t, the compression corner can be selected as an arbitrary point on the curve defined by $f_1 = 0$. We impose the volumetric component of the compression corner point as ξ_m so that the deviatoric component ρ_m can be determined from the condition $f_1 = 0$. Therefore, the yield function for the mixed zone can be expressed as

$$f_2 = \frac{1}{f_c}\left(\rho - \frac{\rho_t - \rho_m}{\xi_t - \xi_m}\,\xi + \frac{\xi_t\,\rho_m - \xi_m\,\rho_t}{\xi_t - \xi_m}\right) \leq 0 \tag{27}$$

If the compression zone or tension cut-off zone is activated during plastic loading, the corner points that define the mixed zone yield function can vary due to the corresponding hardening/softening parameters κ_1 and κ_3, i.e.

$$\xi_t = \xi_t(\kappa_3) \tag{28}$$

$$\rho_m = \rho_m(\kappa_1) \tag{29}$$

Furthermore, the compression corner point is also kept variable, i.e.

$$\xi_m(\kappa_2) = \xi_{m0} - (1 - q_2)\,\xi_{t0} \tag{30}$$

in which ξ_{m0} is the initial volumetric stress at the compression corner CC.

4.3.2 Softening law

The softening law for the mixed zone is selected the same as that of the tension cut-off zone, i.e.

$$\kappa_2 = \kappa_3, \qquad q_2(\kappa_2) = q_3(\kappa_3) \tag{31}$$

4.3.3 Damage Evolution

The damage evolution for the mixed zone is selected the same as that of the tension cut-off zone, i.e.

$$\varphi_2(\kappa_2) = \varphi_3(\kappa_3) \tag{32}$$

4.4 Coupling of internal hardening variables

It is well known that ASR affected concrete exhibit reduction in both compressive strength and stiffness. To represent the deterioration effects, a coupling method is proposed between the plastic hardening variables of compression and tension modes, i.e.

$$\kappa_1 = \gamma\,\kappa_3 \tag{33}$$

in which γ is a coupling factor. Note that the coupling is applied for Stage 1 – the ASR progression case only. Eq. (33) allows for the progression of compressive damage and strength reduction during Stage 1 analysis.

5. NUMERICAL EXAMPLES

In this section, numerical analysis results are presented to illustrate the capabilities of the proposed model. Two examples, one for material-level and one for structural-level investigations, are presented. For both cases, the following procedure is applied:

1. Stage 1: ASR progress stage: The analysis starts with the gradual application of free ASR expansion $\boldsymbol{\varepsilon}_{ASR}^{Free}$ and ASR stress $\boldsymbol{\sigma}_{ASR}$ that cause expansion as well as the evolution of inelastic (plastic-damage) internal variables. When this stage is completed, the analysis model reaches its ultimate expansion. It should be noted that for a free element, the resulting expansion is the same as that prescribed for ASR expansion and no macroscopic stress occurs ($\boldsymbol{\sigma} = 0$). However, the internal ASR pressure $\boldsymbol{\sigma}_{ASR}$ causes effective stress $\boldsymbol{\sigma}_{eff}$ on CEPD, and therefore inelastic internal variables (i.e. κ and φ) evolve. On the hand, for a restrained element case (i.e. concrete with steel reinforcement), the expansion of concrete can produce stresses that are self-equilibrated in the macroscopic level.
2. Stage 2: External loading stage: The analysis continues by the gradual application of the external loads on the structural system in which plasticity and damage variables have already evolved in the previous stage. Therefore, the analysis continues based on non-virgin mechanical properties.

The concrete material parameters used in the examples are shown in Table 5.1 in which Young's modulus E_c, uniaxial compressive strength f_c, uniaxial tensile strength f_t, Poisson ratio ν, the stress at the onset of plastic flow k_o, tensile softening parameter n_3, the damage parameters for a) compression (C_1) and b) tension (C_3), tension cut-off stress components ξ_{t0}, ρ_{t0} and ξ_{m0}, and slope coefficient B of plastic potential function are given. All units are in N and mm.

Table 5.1: Common concrete parameters used in the examples

Example	E_c MPa	f_c MPa	f_t MPa	ν	k_o	n_3	C_1	C_3	ξ_{t0} MPa	ρ_{t0} MPa	ξ_{m0} MPa	B
1	31,000	28	$= 0.09f_c$	0.2	0.14	0.00027	0.355	4850	$= 1.45f_t$	0.2	2.5	4.5
2	37,251	60	$= 0.09f_c$	0.2	0.14	0.00027	0.355	4850	$= 1.45f_t$	0.2	2.5	4.5

5.1 Example1: Material level

In the first example, the variation of mechanical properties of concrete due to ASR deterioration is investigated. For this purpose, a single concrete element under uniaxial compression is considered, and the stress-strain curves obtained from the model are presented in Figure 5.1. Applying the two-stage analysis procedure explained above, the reductions both in modulus of elasticity and compressive strength are be obtained. Free ASR expansion strain of $\boldsymbol{\varepsilon}_{ASR}^{Free} = 0.001$ and coupling factor of $\gamma = 35$ is applied for this example. The reduction in compressive strength is in the order of 14% whereas the reduction in modulus of elasticity is 57%.

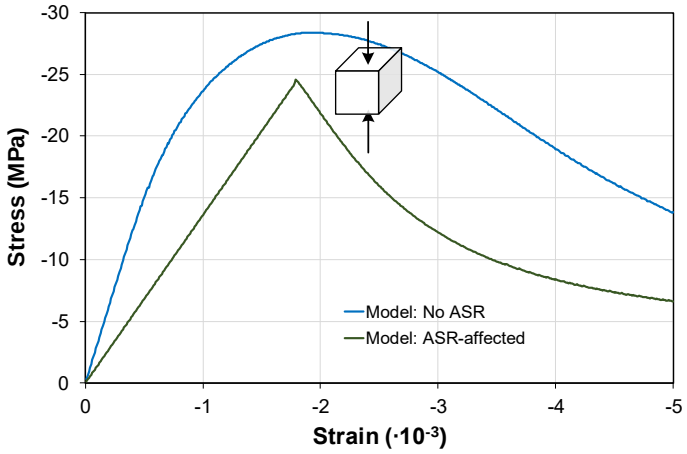

Figure 5.1: Effect of ASR on the uniaxial compressive stress-strain behaviour of concrete

It should be noted that, in contrast with some other methods in the literature i.e. [4], no 'external' reduction factors are applied to strength and elasticity modulus parameters here. On the contrary, the reductions are obtained directly from the constitutive model. It is also remarkable that the reductions in compressive strength and elastic modulus are in agreement with the studies based on experimental observations [22]. This outcome supports the notion that the damage in concrete due to ASR is governed by the mechanical behaviour of the concrete skeleton, as suggested by Ulm et al. [6]. Therefore, a correlation is expected between stiffness and strength reduction of ASR-affected concrete.

5.2 Example 2: Structural level

In the second example, the load-deformation response of a reinforced concrete beam is investigated. The ASR-affected beam experiments given in [23] is considered for this example. The geometry, reinforcement arrangement, load application points and supports are shown in Figure 5.2. Material properties of reinforcing steel is taken as $f_y = 560$ MPa for the yield stress and $E_s = 200{,}000$ MPa for Young's modulus. The steel is assumed as perfectly plastic. Free ASR expansion strain of $\boldsymbol{\varepsilon}_{ASR}^{Free} = 0.016$ and coupling factor of $\gamma = 0.1$ is applied for this example. The results obtained for the non-reactive control beam (B1) and the reactive beam (B2) given in [23] are investigated. For finite element modelling of concrete parts, 3-dimensional solid elements are utilised whereas 2-dimensional bar elements are used for modelling of steel reinforcements.

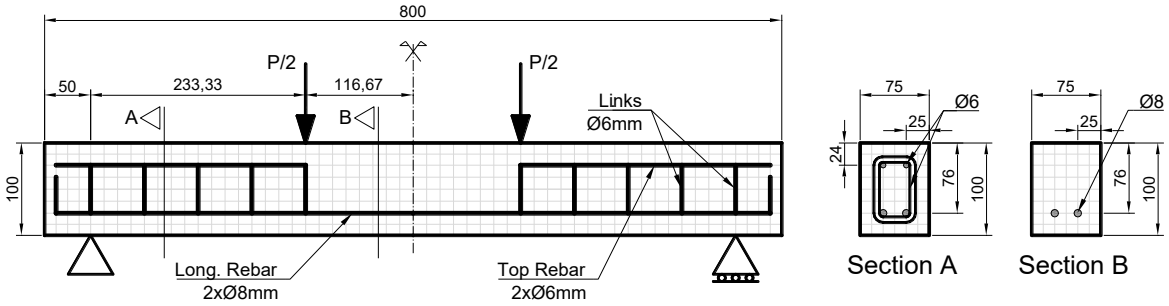

Figure 5.2: Beam experiment details [23]

In the first stage of analysis, no external loads but only ASR effects (volumetric expansion and ASR stress) are applied. Similar to experimental behaviour in [23], the hogging phenomenon is observed from the model at this ASR-only stage. Subsequently, the second stage analysis is performed on the beam by applying external loads, and load-vertical deflection (mid-span) results obtained from the model are compared with the experimental results in Figure 5.3. It should be noted that the deflections are plotted by considering Stage 2 only, similar to given in [23]. Therefore, plotted deflections are not absolute but relative to the final deflections obtained from Stage 1.

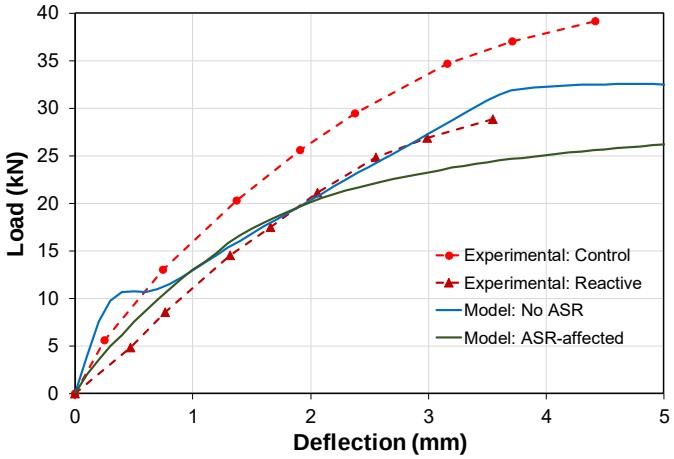

Figure 5.3: Load-deflection response of a beam: Comparison with Swamy, Al-Asali [23]

As shown in Figure 5.3, the essential behaviour, i.e., the reduction in strength and stiffness can be obtained from the model. Considering the lack of data in the experimental work (i.e. strength, Poisson ratio, modulus of elasticity of concrete and stress-strain curve of reinforcing steel), the majority of material properties to be used in the model are selected by employing approximations based on the mix design of concrete and typical reinforcing steel properties. Therefore, in this study, rather than their absolute values, the differences between control and ASR-affected beams are investigated. While the reduction in the initial load-deflection slope is measured as 54% for the experimental data, the corresponding reduction obtained from the model is 49%. Similarly, the reduction in load-carrying capacity is 21% and 22% for the experimental and model results, respectively. Note that in the latter comparison, the differences are measured from the last data point for experimental data (3.55 mm deflection) and at where steel yields (3.60 mm deflection) for the model results, in order to eliminate the potential effects of steel hardening on the global behaviour.

6. CONCLUSIONS

The coupled elastoplastic-damage model (CEPD) given in [15] can simulate concrete's inelastic behaviour under triaxial compression, and it has been improved in [16] to cover the behaviour under uniaxial tensile stresses. In this study, by introducing a novel three-surface plasticity framework, we have extended the capabilities of the CEPD, and it can capture the inelastic response of concrete in any stress state, whether it has a compressive or tensile character.

In order to simulate the mechanical behaviour of ASR-affected concrete elements, the CEPD is utilised as the main part of the constitutive model. The CEPD is considered in the mesoscale, and the ASR-induced internal pressure is adopted as an eigenstress, which self-equilibrates in the macroscale but can influence the material behaviour due to interactions at meso-scale. Therefore, the proposed model, representing the sub-scale mechanisms, can provide an efficient way to consider the ASR related damages at the structural scale.

In the material level, it is shown that our novel CEPD-ASR model can be utilised to predict reductions in both strength and stiffness. The deteriorated material properties are obtained as an outcome of the model. Numerous models in the literature, i.e. [24,25], introduce external *strength reduction factors* to capture this phenomenon.

Since the model is based on the *effective stress* notion, the presence of stresses can inhibit or magnify the deterioration on the material, depending on the stress-state. Therefore, the proposed model is capable of simulating the *stress dependency* phenomenon observed in ASR-affected concrete.

It is also shown that our novel CEPD-ASR model can capture the essential behaviour of ASR-affected structural elements. Solid finite elements are appropriate for modelling of ASR-affected structural components because they incorporate triaxial elastoplastic-damage material models to capture the effects of confinement and its interactions with volumetric expansion, using minimal calibration. Simpler 1D modelling approaches commonly used for civil structures such as bridge beams cannot incorporate those 3D considerations of the material behaviour unless some ad-hoc adjustments are introduced based on the loading and ASR expansion case.

7. ACKNOWLEDGEMENT

This research is funded through an Australian Research Council Research Hub for Nanoscience Based Construction Materials Manufacturing (NANOCOMM) with the support of the Transport for New South Wales (TfNSW). The authors are grateful for the financial support of the Australian Research Council (IH150100006) in conducting this study.

8. REFERENCES

[1] Comi C, Fedele R, Perego U (2009) A chemo-thermo-damage model for the analysis of concrete dams affected by alkali-silica reaction. Mechanics of Materials 41 (3):210-230. doi:https://doi.org/10.1016/j.mechmat.2008.10.010

[2] Farage MCR, Alves JLD, Fairbairn EMR (2004) Macroscopic model of concrete subjected to alkali–aggregate reaction. Cement and Concrete Research 34 (3):495-505. doi:10.1016/j.cemconres.2003.09.001

[3] Grimal É, Sellier A, Le Pape Y, Bourdarot É (2008) Creep, shrinkage, and anisotropic damage in alkali-aggregate reaction swelling mechanism-Part I: A constitutive model. ACI Materials Journal 105 (3):227

[4] Huang M, Pietruszczak S (1999) Modeling of thermomechanical effects of alkali-silica reaction. Journal of Engineering Mechanics 125 (4):476

[5] Ulm F-J, Coussy O, Kefei L, Larive C (2000) Thermo-chemo-mechanics of ASR expansion in concrete structures. Journal of Engineering Mechanics 126 (3):233-242. doi:doi:10.1061/(ASCE)0733-9399(2000)126:3(233)

[6] Ulm F-J, Peterson M, Lemarchand E (2002) Is ASR-expansion caused by chemoporoplastic dilatation? Concrete Science and Engineering 4 (13):47-55

[7] Pan JW, Feng YT, Wang JT, Sun QC, Zhang CH, Owen DRJ (2012) Modeling of alkali-silica reaction in concrete: a review. Frontiers of Structural and Civil Engineering 6 (1):1-18. doi:10.1007/s11709-012-0141-2

[8] Esposito R, Hendriks MAN (2017) Literature review of modelling approaches for ASR in concrete: A new perspective. European Journal of Environmental and Civil Engineering:1-21. doi:10.1080/19648189.2017.1347068

[9] Comi C, Perego U (2011) Anisotropic Damage Model for Concrete Affected by Alkali-Aggregate Reaction. International Journal of Damage Mechanics 20 (4):598-617. doi:10.1177/1056789510386857

[10] Červenka J, Papanikolaou VK (2008) Three dimensional combined fracture–plastic material model for concrete. International Journal of Plasticity 24 (12):2192-2220

[11] Grassl P, Jirásek M (2006) Damage-plastic model for concrete failure. International Journal of Solids and Structures 43 (22-23):7166-7196. doi:10.1016/j.ijsolstr.2006.06.032

[12] Lee J, Fenves GL (1998) Plastic-damage model for cyclic loading of concrete structures. Journal of Engineering Mechanics 124 (8):892-900. doi:https://doi.org/10.1061/(ASCE)0733-9399(1998)124:8(892)

[13] Meschke G, Lackner R, Mang HA (1998) An anisotropic elastoplastic-damage model for plain concrete. International Journal for Numerical Methods in Engineering 42 (4):703-727

[14] Armero F, Oller S (2000) A general framework for continuum damage models. I. Infinitesimal plastic damage models in stress space. International Journal of Solids and Structures 37 (48):7409-7436

[15] Sarikaya A, Erkmen RE (2019) A plastic-damage model for concrete under compression. International Journal of Mechanical Sciences 150:584-593. doi:https://doi.org/10.1016/j.ijmecsci.2018.10.042

[16] Sarikaya A, Erkmen RE, Gowripalan N, Sirivivatnanon V, South W (2019) A plastic-damage model for concrete under cyclic loads. Paper presented at the Concrete 2019, Sydney, Australia, 2019/09/11

[17] Ibrahimbegović A, Markovič D, Gatuingt F (2003) Constitutive model of coupled damage-plasticity and its finite element implementation. Revue Européenne des Eléments Finis 12 (4):381-405

[18] Simo JC, Kennedy JG, Govindjee S (1988) Non-smooth multisurface plasticity and viscoplasticity. Loading/unloading conditions and numerical algorithms. International Journal for Numerical Methods in Engineering 26 (10):2161-2185. doi:doi:10.1002/nme.1620261003

[19] Jirásek M (2002) Inelastic analysis of structures. Wiley, Chichester, West Sussex, England ;

[20] Menetrey P, Willam KJ (1995) Triaxial failure criterion for concrete and its generalization. Structural Journal 92 (3):311-318

[21] Papanikolaou VK, Kappos AJ (2007) Confinement-sensitive plasticity constitutive model for concrete in triaxial compression. International Journal of Solids and Structures 44 (21):7021-7048

[22] IStructE (1992) Structural effects of alkali-silica reaction. Technical guidance on the apprasial of existing structures. The Institution of Structural Engineers (IStructE), London, U.K.

[23] Swamy RN, Al-Asali MM (1989) Effect of alkali-silica reaction on the structural behavior of reinforced concrete beams. Structural Journal 86 (4):451-459

[24] Saouma VE, Perotti L (2006) Constitutive model for alkali-aggregate reactions. ACI Materials Journal 103 (3):194-202

[25] Winnicki A, Pietruszczak S (2008) On mechanical degradation of reinforced concrete affected by alkali-silica reaction. Journal of Engineering Mechanics 134 (8):611-627. doi:10.1061/(ASCE)0733-9399(2008)134:8(611)

A plastic-damage model for concrete affected by alkali-silica reaction
Atila Sarikaya; Emre Erkmen; Nadarajah Gowripalan; Vute Sirivivatnanon